

# Seasonality and declining intensity of methane emissions from the Permian and nearby US oil and gas basins

*Daniel J. Varon<sup>1</sup> ([danielvaron@g.harvard.edu](mailto:danielvaron@g.harvard.edu)), Daniel J. Jacob<sup>1</sup>, Lucas A. Estrada<sup>1</sup>, Nicholas Balasus<sup>1</sup>, James D. East<sup>1</sup>, Drew C. Pendergrass<sup>1</sup>, Zichong Chen<sup>1</sup>, Melissa Sulprizio<sup>1</sup>, Mark Omara<sup>2</sup>, Ritesh Gautam<sup>2</sup>, Zachary R. Barkley<sup>3</sup>, Felipe J. Cardoso-Saldaña<sup>4</sup>, Emily K. Reidy<sup>4</sup>, Harshil Kamdar<sup>5,6</sup>, Evan D. Sherwin<sup>7</sup>, Sebastien C. Biraud<sup>7</sup>, Dylan Jervis<sup>8</sup>, Sudhanshu Pandey<sup>9</sup>, John R. Worden<sup>9</sup>, Kevin W. Bowman<sup>9</sup>, Joannes D. Maasakkers<sup>10</sup>, Robert L. Kleinberg<sup>11</sup>*

<sup>1</sup> Harvard University, School of Engineering and Applied Science

<sup>2</sup> Environmental Defense Fund

<sup>3</sup> The Pennsylvania State University, Department of Meteorology and Atmospheric Science

<sup>4</sup> ExxonMobil Technology and Engineering Company

<sup>5</sup> Insight M

<sup>6</sup> Harvard University, Salata Institute for Climate and Sustainability

<sup>7</sup> Lawrence Berkeley National Laboratory

<sup>8</sup> GHGSat, Inc.

<sup>9</sup> Jet Propulsion Laboratory, California Institute of Technology

<sup>10</sup> SRON Space Research Organisation Netherlands

<sup>11</sup> Columbia University Center on Global Energy Policy

Keywords: Permian, methane, seasonality, TROPOMI

## **Abstract**

We quantify weekly methane emissions and trends from oil and gas production in the US Permian Basin for 2019–2023, and in nearby basins for 2022–2023, by analytical inversion of Tropospheric Monitoring Instrument (TROPOMI) satellite observations with the Integrated Methane Inversion (IMI) at 25-km resolution. Permian oil and gas emissions averaged  $4.0 \pm 1.1 \text{ Tg a}^{-1}$  over 2019–2023, with large seasonal variation but little interannual variability. Methane intensity fell from 5.2% to 3.2% as production surged. Intensity in the New Mexico Permian fell from 5.7% to 2.6%, approaching the state’s 2026 target of <2%. Emissions were on average 60% higher in the winter than summer, which we corroborate with Permian Basin Tower Network measurements, Insight M aircraft data, and GHGSat satellite observations. This seasonality may be driven in part by higher winter emissions from liquid storage tanks due to decreased separator efficiency in cold conditions. Similar but weaker seasonality along with decreasing emissions and intensities is found in weekly inversions for the Anadarko, Barnett, Eagle Ford, and Haynesville basins in 2022–2023. Our work suggests that better weatherization of oil and gas facilities could significantly reduce methane emissions.

## **Synopsis**

Satellite observations reveal strong seasonal variability and declining intensity of methane emissions from the Permian and nearby US oil and gas basins.

## 1 Introduction

Curbing methane emissions is a powerful lever for slowing near-term warming. Anthropogenic methane emissions come from a wide range of activities in the agriculture, fossil fuel, and waste sectors. Emissions from oil and gas production have been identified as a priority for mitigation because the captured gas can be sold and because relatively few actors control the means of production. Satellite observations of atmospheric methane offer a means to quantify emissions and their trends in oil and gas production regions worldwide<sup>1,2</sup>. The TROPOspheric Monitoring Instrument (TROPOMI) aboard the Sentinel-5P satellite provides a uniquely dense record of global methane concentrations with up to  $7 \times 5.5\text{-km}^2$  pixel resolution and daily global coverage from May 2018 to present<sup>3,4</sup>. This dense spatiotemporal sampling lends itself to high-frequency monitoring of methane emissions at regional scales<sup>5</sup> and could be of great value for tracking mitigation efforts.

The Permian Basin in Texas and New Mexico is a prolific oil and gas province that accounts for more than 40% of US oil production<sup>6</sup>. Strong methane emissions from Permian oil and gas activities have been extensively documented by satellite<sup>7,8</sup>, aircraft<sup>9,10</sup>, and ground measurement platforms<sup>11</sup>. The methane intensity of Permian oil and gas production, defined as the ratio of emitted to marketed gas across the basin, is much higher than the Oil and Gas Climate Initiative (OGCI) industry target of  $<0.2\%$ <sup>12</sup>, with estimates in the literature ranging from  $\sim 3\%$  to more than 9% depending on the study region and period<sup>7,10,13</sup>. There has been strong interest in monitoring Permian methane emissions over time to improve understanding of their drivers and to determine whether emissions and intensity are decreasing. Lu et al. (2023)<sup>14</sup> inferred annual Permian methane emissions from 2010 to 2019 from GOSAT satellite observations and reported a decrease in intensity from 7% to 3%. Varon et al. (2023)<sup>15</sup>

demonstrated weekly continuous monitoring of Permian methane emissions with TROPOMI from May 2018 through October 2020 and also reported decreasing intensity, from 6% to 3%. The intensity decreases were due to emissions remaining flat while production increased, and gas prices and drilling of new wells were better predictors of emissions than production.

Here we extend the weekly analysis of Varon et al. (2023)<sup>15</sup> to five full years, from 2019 to 2023, to evaluate more recent trends in Permian methane emissions and intensity, and to analyze a large, unexpected seasonality in emissions that corroborates recent findings by Vanselow et al. (2024)<sup>16</sup> and Hu et al. (2025)<sup>17</sup>. We use the open-source Integrated Methane Inversion (IMI) framework<sup>18,19</sup> to infer weekly emissions at  $0.25^\circ \times 0.3125^\circ$  ( $\approx 25$ -km) resolution from TROPOMI satellite observations. We evaluate our results with independent methane measurements from the Permian Basin Tower Network, and from Insight M aerial surveys and GHGSat satellite observations of methane point sources. We also perform weekly methane inversions over two years (2022–2023) for four other high-emitting oil and gas basins in the south-central United States—the Anadarko, Barnett, Eagle Ford, and Haynesville basins—to compare emissions and trends with those in the Permian.

## 2 Materials and Methods

The IMI is an open-source cloud-computing facility for inferring methane emissions at up to 25-km resolution for any region and period of interest based on an analytical Bayesian inverse analysis of TROPOMI satellite observations. It is available as a free product on the Amazon Web Services (AWS) cloud and can be downloaded and run locally. IMI 2.0 introduced a capability for users to continuously monitor emissions from a region of interest using a Kalman filter with user-selected update frequency (e.g., weekly, monthly)<sup>15,19</sup>. We describe our configuration of the IMI Kalman filter in more detail below.

## 2.1 TROPOMI satellite observations

We use satellite observations of column-average methane mixing ratio  $X_{\text{CH}_4}$  [ppb] from the Balasus et al. (2023)<sup>20</sup> blended TROPOMI+GOSAT retrieval product. The blended product uses a machine learning model to correct differences between TROPOMI and GOSAT observations based on predictor variables from the operational (v02.04.00) TROPOMI retrieval. The model is trained on more than 150,000 pairs of co-located TROPOMI and GOSAT observations and adjusts TROPOMI to be more consistent with the GOSAT data, which are about 200 times sparser than TROPOMI but less prone to artifacts. It shows improved agreement with the Total Column Carbon Observing Network (TCCON) relative to the operational TROPOMI product in terms of variable bias ( $<5$  ppb) and precision ( $<12$  ppb)<sup>20</sup>.

Figure 1 shows the Permian, Anadarko, Barnett, Eagle Ford, and Haynesville regions of interest for our inversions, along with prior emission estimates and a sample week of TROPOMI observations. Weekly observation counts  $m$  (mean  $\pm$  standard deviation) range from  $627 \pm 582$  for the Haynesville Basin to  $5117 \pm 3143$  for the Permian. TROPOMI observations are lacking for 28 July – 18 August 2022 and 10–24 August 2023 due to failure of the VIIRS instrument, which provides cloud masks for the TROPOMI methane retrieval<sup>21</sup>.

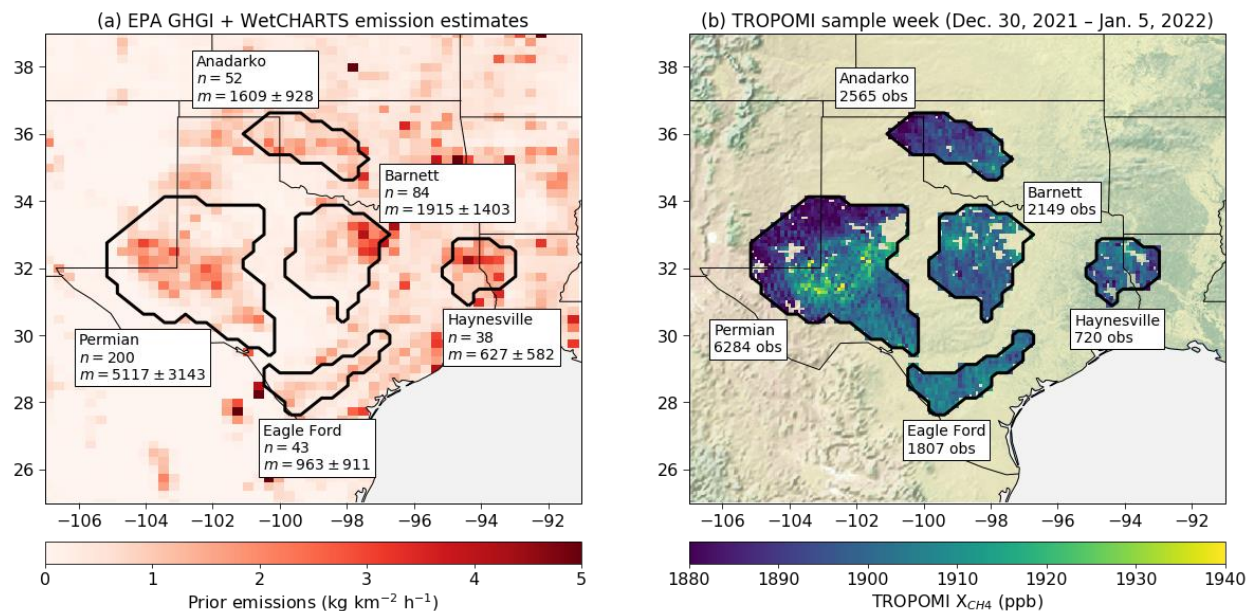


**Figure 1:** Oil and gas production regions in the south-central US. (a) 2020 bottom-up methane emission estimates on the  $0.25^\circ \times 0.3125^\circ$  GEOS-Chem grid from the gridded version of the US EPA Greenhouse Gas Inventory (GHGI) version 2 Express Extension<sup>22</sup> and from the mean of the WetCHARTS v1.3.1 wetlands inventory ensemble<sup>23</sup>. The black contours delineate the regions of interest optimized in the inversion with the state vector consisting of the  $0.25^\circ \times 0.3125^\circ$  grid cells. Text insets give the number of state vector elements  $n$  and the weekly average number ( $\pm$  standard deviation) of TROPOMI observations  $m$  over the 2019–2023 period. (b) Blended TROPOMI+GOSAT  $X_{\text{CH}_4}$  observations<sup>20</sup>, referred to in the text as TROPOMI, averaged over a typical sample week (December 30, 2021 – January 5, 2022) on a  $0.1^\circ \times 0.1^\circ$  grid, with the number of observations indicated for each region of interest.

## 2.2 GEOS-Chem forward model

The IMI uses the nested GEOS-Chem chemical transport model (here v14.2.3)<sup>24</sup> as the forward model for regional inversions. The model is driven by assimilated meteorological data from NASA’s Goddard Earth Observing System Forward Processing (GEOS-FP) product. It has  $0.25^\circ \times 0.3125^\circ$  resolution and 47 vertical layers, reduced from the 72 native layers of GEOS-FP by combining layers in the upper stratosphere and mesosphere. Boundary conditions for the nested domain are from a global boundary condition dataset distributed with the IMI, which is based on a  $2^\circ \times 2.5^\circ$  GEOS-Chem simulation corrected to match spatiotemporally smoothed TROPOMI observations<sup>18,19</sup>. The model is initialized from a 1-month spin-up simulation using the boundary condition dataset as initial conditions.

The IMI uses a TROPOMI observation operator to sample the 3D GEOS-Chem methane output fields at the locations and times of the TROPOMI observations<sup>18</sup>. This generates pseudo-observations for comparison with the real ones. The IMI TROPOMI operator accounts for variable footprint geometry and vertical averaging kernel vectors as reported in the operational TROPOMI retrieval product. In IMI 2.0, individual TROPOMI observations are averaged by orbit into super-observations on the  $0.25^\circ \times 0.3125^\circ$  GEOS-Chem grid for computational expediency and better accounting of errors.

### **2.3 Prior emission estimates**

We use the default IMI 2.0 prior emission estimates described by Estrada et al. (2025)<sup>19</sup> and shown in Figure 1. Anthropogenic emissions are from the gridded version of the US Environmental Protection Agency (EPA) Greenhouse Gas Inventory (GHGI), version 2 Express Extension<sup>22</sup>. Wetland emissions are from the WetCHARTS v1.3.1 ensemble mean<sup>23</sup> and fire emissions are from GFED4<sup>25</sup>. Emissions from geological seeps are from Etiope et al. (2019)<sup>26</sup> scaled to  $2 \text{ Tg a}^{-1}$  following Hmiel et al. (2020)<sup>27</sup>. Emissions from termites are from Fung et al. (1991)<sup>28</sup>. Methane losses from soil absorption and oxidation by OH and Cl are included in the GEOS-Chem forward model through prescribed oxidant concentration fields and the MeMo soil methanotrophy model<sup>29</sup>. Losses are relatively uniform across our regional inversion domains and are thus effectively optimized through correction to the boundary conditions as described in the next section.

### **2.4 State vectors**

The black contours in Figure 1 outline the emission state vectors (2D gridded methane emissions) optimized in our inversions. The emission state vectors have native 25-km resolution within the basin boundaries. They also include 16 coarse buffer elements (not shown in Figure

1), which are collections of 25-km grid cells outside the region of interest that serve to adjust external emissions and pad out the rectangular inversion domain<sup>18,30</sup>.

Regional inversions are sensitive to errors in the boundary conditions, which can alias into the solution for emissions. While the buffer emission elements provide some protection against this, and the TROPOMI boundary conditions dataset is on average unbiased, we also optimize the boundary conditions directly in our inversions by including in the state vector four additional elements representing adjustments to be applied to the methane concentrations along the edges of the inversion domain. The state vectors for our weekly inversions thus contain  $n + 16 + 4$  elements:  $n$  high-resolution emission elements within the region of interest (shown inset in Figure 1), 16 coarse buffer emission elements outside the region of interest, and 4 boundary condition elements along the cardinal edges of the domain.

## 2.5 Inversion

We use the IMI 2.0 continuous emission monitoring (Kalman filter) feature developed by Varon et al. (2023)<sup>15</sup> and Estrada et al. (2025)<sup>19</sup> to infer weekly methane emissions from our regions of interest. For a given week and region, we seek to optimize the state vector  $\mathbf{x}$  (emissions and boundary conditions) to better match the satellite observations  $\mathbf{y} = \mathbf{F}(\mathbf{x}) + \boldsymbol{\epsilon}$  by inverting the forward model  $\mathbf{F}$  while accounting for model and observation errors  $\boldsymbol{\epsilon}$ . The problem is generally underconstrained due to observational errors and gaps in coverage, which can be addressed by regularizing the solution with prior estimates  $\mathbf{x}_A$ . Assuming normally distributed error pdfs on  $\mathbf{x}$  and  $\mathbf{y}$ , the problem is then to minimize the cost function<sup>31</sup>

$$J(\mathbf{x}) = (\mathbf{x} - \mathbf{x}_A)^T \mathbf{S}_A^{-1} (\mathbf{x} - \mathbf{x}_A) + \gamma (\mathbf{y} - \mathbf{K}\mathbf{x})^T \mathbf{S}_o^{-1} (\mathbf{y} - \mathbf{K}\mathbf{x}), \quad (1)$$

where  $\mathbf{K} = d\mathbf{F}/d\mathbf{x}$  is the Jacobian matrix representing the sensitivity of the observations to the state variables,  $\mathbf{S}_A$  is a prior error covariance matrix describing uncertainties in the prior estimates,  $\mathbf{S}_o$  is an observational error covariance matrix describing the combined model and observation errors, and  $\gamma$  is a regularization parameter to prevent overfitting in the solution. We use the default IMI 2.0 settings for these parameters, taking  $\mathbf{S}_A$  and  $\mathbf{S}_o$  to be diagonal with uniform error standard deviations  $\sigma_A = 50\%$  for emissions ( $\sigma_A = 10$  ppb for boundary conditions) and  $\sigma_o = 15$  ppb<sup>19</sup> for observations (scaled down for super-observations following Chen et al., 2023<sup>32</sup>). The number of observations over a weekly period is sufficiently small that overfitting is not a concern and so we set  $\gamma = 1$ . The optimized (posterior) emissions  $\hat{\mathbf{x}}$  are obtained analytically by solving  $dJ(\mathbf{x})/d\mathbf{x} = \mathbf{0}$  for  $\mathbf{x}$ :

$$\hat{\mathbf{x}} = \mathbf{x}_A + (\gamma\mathbf{K}^T\mathbf{S}_o^{-1}\mathbf{K} + \mathbf{S}_A^{-1})^{-1}\gamma\mathbf{K}^T\mathbf{S}_o^{-1}(\mathbf{y} - \mathbf{K}\mathbf{x}_A). \quad (2)$$

In the IMI 2.0 Kalman filter inversion, the prior estimates  $\mathbf{x}_A$  evolve from week to week based on the latest posterior solution in combination with the original prior estimate<sup>15</sup>:

$$\mathbf{x}_A^i = \lambda(\alpha\mathbf{x}_A^0 + (1 - \alpha)\hat{\mathbf{x}}^{i-1}). \quad (3)$$

Here  $\mathbf{x}_A^i$  is the prior estimate for the current week  $i \geq 1$ ,  $\mathbf{x}_A^0$  is the original prior estimate,  $\hat{\mathbf{x}}^{i-1}$  is the most recent weekly posterior estimate (with  $\hat{\mathbf{x}}^0 = \mathbf{x}_A^0$ ),  $\alpha = 0.1$  assigns 10% weight to the original prior and 90% weight to the most recent posterior, and  $\lambda$  is a scale factor to ensure that  $\mathbf{x}_A^i$  has the same mean emission as  $\hat{\mathbf{x}}^{i-1}$ . This update is applied only to emissions within the region of interest; prior estimates for buffer emission elements are not updated from week to week, and prior estimates for the boundary conditions follow the time-dependent IMI boundary

condition dataset. If no observations are available during week  $i$ , the inversion returns  $\hat{\mathbf{x}}^i = \mathbf{x}_A^i$ .

The posterior distribution of source sectors in each grid cell follows that of the prior.

IMI 2.0 provides an option to use lognormal error pdfs for emissions in the inversion<sup>19</sup>, which has the advantage of enforcing positivity in the posterior emission solution and reflects the well-documented heavy tail of methane emissions<sup>33</sup>. We use this option in our inversions for the Permian Basin. With lognormal errors, Equation (1) is solved in log space ( $\mathbf{x} \rightarrow \mathbf{x}' = \ln \mathbf{x}$ ) and becomes nonlinear, so that the Jacobian matrix ( $\mathbf{K} \rightarrow \mathbf{K}' = d\mathbf{F}/d \ln \mathbf{x}$ ) must be updated iteratively to converge to a solution. IMI 2.0 uses the Levenberg-Marquardt optimization algorithm as described by Rodgers (2000)<sup>34</sup> for this purpose. We only optimize the emissions within the region of interest in log space; the boundary condition and buffer emission elements of the state vector are optimized with normally distributed error pdfs, because they are intended to correct boundary condition errors and need not be strictly positive. The prior emission error covariances in the lognormal inversion become geometric error variances  $(\ln \sigma_g)^2$ , where  $\sigma_g$  is the geometric error standard deviation. We set  $\sigma_g = 2$ , reflecting a factor-of-two uncertainty in the prior emission estimates.

While the normal inversion solves for the mean of a Gaussian distribution, the lognormal inversion solves for the median of a lognormal distribution. The prior estimates  $\mathbf{x}_A$ , which reflect mean emission values, therefore need to be adjusted to reflect medians, and the IMI does so following Hancock et al. (2025)<sup>35</sup>, by applying the formula

$$x_{\text{median}} = x_{\text{mean}} \exp\left(-\frac{(\ln \sigma_g)^2}{2}\right) \quad (4)$$

such that  $\mathbf{x}_A \rightarrow \mathbf{x}'_A = 0.79 \ln \mathbf{x}_A$ . The reverse correction is then applied to the posterior emission solution to recover a mean value that can be compared with the prior inventory estimates.

### 3 Results and Discussion

#### 3.1 Permian methane emissions and intensity

Figure 2 shows time series of total oil and gas methane emissions, gas production, active well count, and methane intensity for the Permian from 2019 to 2023. Our inversions begin in July 2018, but we discard the first six months of results as a burn-in period to address low bias in the EPA GHGI (our prior estimate), which reports Permian methane emissions of only  $1.1 \text{ Tg a}^{-1}$  with  $0.9 \text{ Tg a}^{-1}$  from oil and gas production. We find that Permian emissions averaged  $4.9 \pm 1.3 \text{ Tg a}^{-1}$  (weekly mean  $\pm$  standard deviation) over the 2019–2023 period, nearly five times higher than the GHGI, with  $4.0 \pm 1.1 \text{ Tg a}^{-1}$  from oil and gas. A strong seasonal variation is apparent in the oil and gas posterior emissions, which are on average nearly 60% higher in the winter (December, January, February; DJF) than summer (June, July, August; JJA), and we discuss it further below.

Interannual variability of emissions is considerably weaker. Emissions fell 14% from 2019 to 2020, likely due to the reduction in new wells entering production during the COVID-19 pandemic<sup>15,36</sup>, but then rebounded with the number of active wells. The large increase in gas production during the study period, nearly a doubling from  $13 \text{ Bcf d}^{-1}$  in early 2020 to  $25 \text{ Bcf d}^{-1}$  by the end of 2023, did not produce a similar trend in emissions. Methane intensity averaged  $4.0\% \pm 1.1\%$  and fell steadily from  $5.2\% \pm 0.8\%$  in 2019 to  $3.2\% \pm 0.9\%$  in 2023. The decline in methane intensity continues to reflect increasing production, not decreasing emissions.

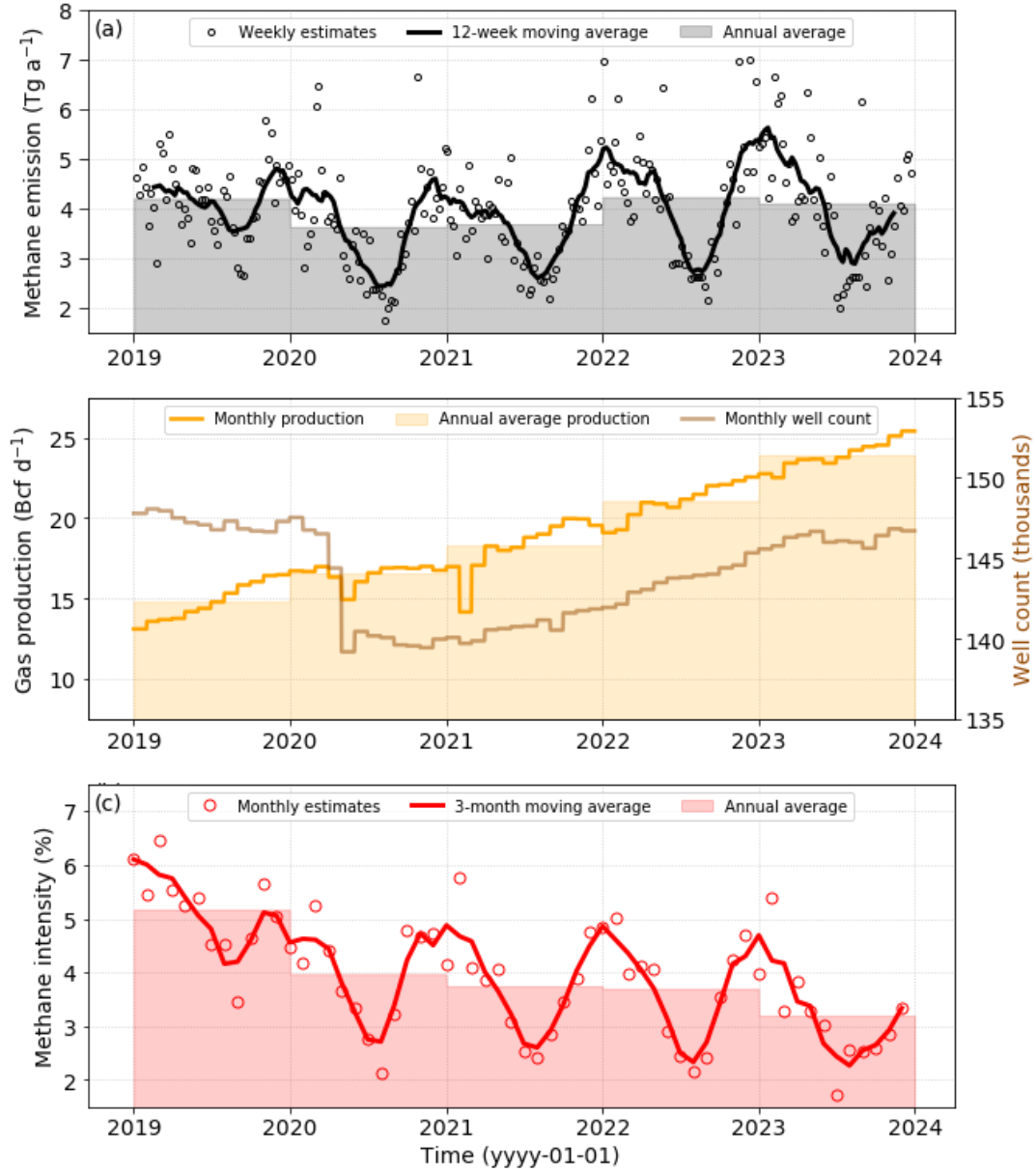


**Figure 2:** Total oil and gas methane emissions, gas production, active well count, and methane intensity for the Permian, 2019–2023. Tick marks on the x-axes indicate January 1 of each year. (a) Weekly methane emissions inferred from TROPOMI data along with 12-week and annual averages. (b) Monthly gas production data and well count from Enverus Drillinginfo<sup>37</sup> along with annual average production. (c) Monthly methane intensity (ratio of methane emitted to methane gas produced) derived from panels (a) and (b) along with 3-month and annual averages, assuming 80% methane content for Permian gas<sup>7</sup>. To compute the monthly intensity, we resample our weekly emission estimates to daily values and then compute monthly emission averages for comparison with the monthly production data.

In 2021 and 2022, New Mexico introduced new state policies to reduce oil and gas methane emissions, requiring that operators achieve methane intensities of less than 2% by 2026<sup>38</sup>, and separately requiring to reduce air pollution from oil and gas activities for better

compliance with the national ambient air quality standard for ozone<sup>39</sup>. We examined whether emissions and intensity declined in response to these policies by separating our posterior emission estimates for Texas and New Mexico (Figure S2). Methane intensity in the New Mexico Permian decreased rapidly during the study period, from  $5.7\% \pm 1.4\%$  in 2019 to  $2.6\% \pm 0.8\%$  in 2023, approaching the state's target of 2% as growth in production outpaced that in emissions. However, most of the decrease occurred before 2021.

### **3.2 Evaluation with independent observations**

Independent observations of methane concentrations in the Permian Basin can verify the emission trends we infer from TROPOMI. We evaluate our results using independent ground-based observations from the Permian Basin Tower Network, aerial surveys of methane point sources from Insight M, and satellite observations of point sources from GHGSat.

#### **3.2.1 Tall tower measurements**

The Permian Basin Tower Network has measured in-situ methane concentrations since March 2020<sup>11,40</sup>. Five towers operated continuously throughout 2022 and 2023. Figure 3a–e compares weekly averages of methane enhancements at each tower with those simulated by the GEOS-Chem forward model using either prior or posterior emissions. The averages are for afternoon hours (20:00–24:00 UTC) when the mixed layer is fully developed<sup>11</sup>. Enhancements are defined relative to a seasonally varying background concentration, which we obtain by fitting the lower envelopes of the observed and simulated time series of methane concentrations at each tower with a natural smoothing spline. At all towers, the posterior GEOS-Chem simulation improves agreement with the observations as diagnosed by the Pearson correlation coefficient  $R$  and root-mean-square error (RMSE). The mean bias improves at all towers except Hobbs.

Figure 3f compares our results with monthly inversions of the tower observations quantifying emissions from a  $\sim 200 \times 200$ -km<sup>2</sup> rectangular domain around the Permian Delaware sub-basin<sup>11</sup>. Mean emissions of 1.7 Tg a<sup>-1</sup> for the towers and 1.9 Tg a<sup>-1</sup> for TROPOMI for the period March 2020 to December 2023 agree to within 10%–15%. The towers suggest a stronger summer 2020 uptick in emissions than TROPOMI and a weaker 2022 winter uptick, but the overall trends are consistent.

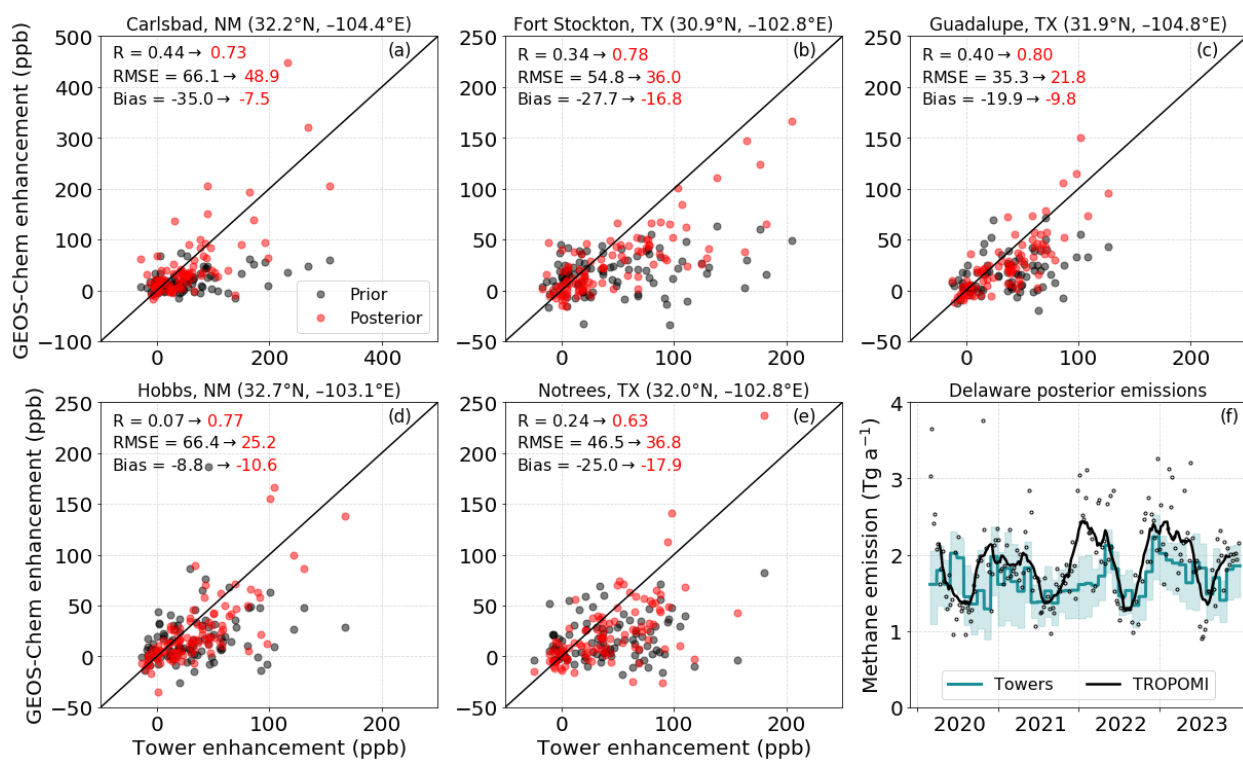


**Figure 3:** Evaluation of our weekly inversions with in-situ methane measurements from the Permian Basin Tower Network. Panels (a–e) compare simulated methane enhancements relative to the seasonal background from GEOS-Chem using prior emissions and posterior (weekly updated) emissions to observations from five tall towers (2022–2023). Enhancements are shown as weekly mean afternoon (20:00–24:00 UTC) values. The insets show the Pearson correlation coefficient  $R$ , root-mean-square error (RMSE), and mean bias. The 1:1 line is shown in black. Panel (f) compares our weekly inversions (black circles, with 12-week moving average as black line) with monthly inversions of the tower observations (blue line, with blue shading showing the range of results from a sensitivity analysis adjusting inversion parameters) described by Barkley et al. (2023)<sup>11</sup> for March 2020 to December 2023. Emissions are for a  $200 \times 200$ -km<sup>2</sup> rectangular domain around the Permian Delaware sub-basin (30.82°N to 32.89°N, -104.99°E to -102.71°E). Tick marks on the x-axis indicate January 1 of each year.

### 3.2.2 Aircraft and satellite observations of methane point sources

Next, we compare our results with methane point source observations from wide-area Insight M aerial remote sensing surveys<sup>41</sup> (Text S1) and targeted GHGSat satellite monitoring<sup>42</sup> (Text S2) in the Permian. The Insight M surveys ran from 2021 to 2023 and covered infrastructure representing 47%–89% of total natural gas production in the Permian depending on the year. We compute total aerially detected emissions per year following the approach of Sherwin et al. (2025)<sup>41</sup> and considering infrastructure surveyed at least once per quarter (Text S1). GHGSat monitored 1041 distinct source locations from 2022 to 2024 with a constellation of 5–10 satellites and detected 1629 plumes from 1098 clear-sky acquisitions targeting domains of size 12×15 to 12×40 km<sup>2</sup>. We applied the methodology of Jervis et al. (2025)<sup>42</sup> to quantify daily emissions and detections per source location from 2022 to 2024 (Text S2; Figure S3). Source locations were defined by attributing to a new location any detected plume origin not within 300 m of another plume origin.

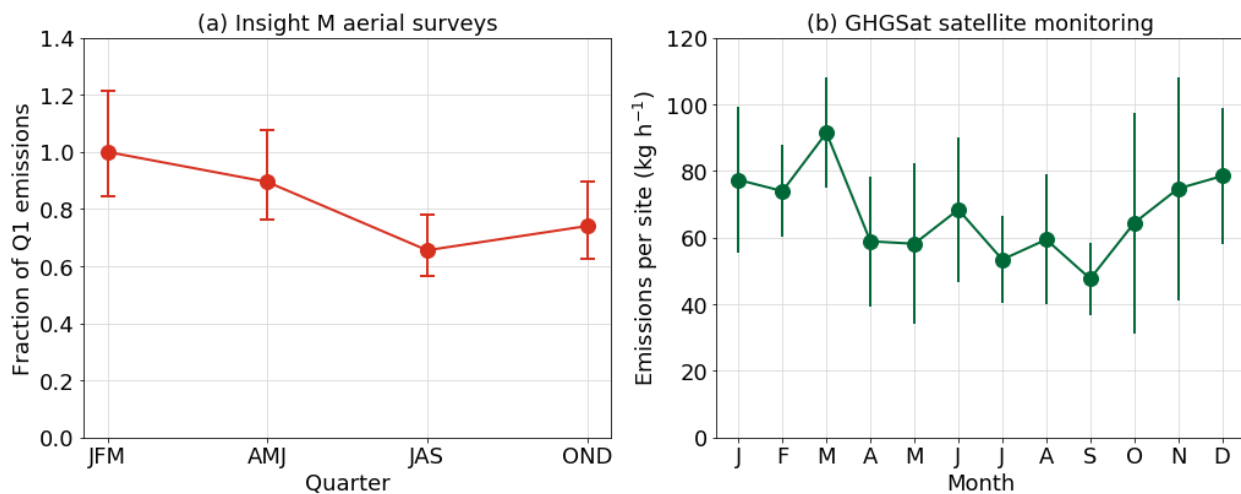


**Figure 4:** Seasonality of Permian point source emissions based on (a) Insight M aerial surveys and (b) targeted GHGSat satellite monitoring of oil and gas infrastructure in the Permian. (a) Quarterly total emissions detected by Insight M from 2021 to 2023<sup>41</sup>, normalized to emissions in the first quarter of each year and averaged over all three years. Error bars represent 95% confidence intervals. (b) Monthly mean emissions per source location monitored by GHGSat from 2022 to 2024<sup>42</sup>. Error bars represent the standard deviation of daily values within each month.

Figure 4 plots the quarterly variability in total point source emissions detected by Insight M from 2021 to 2023, and the monthly variability in total emissions per source location monitored by GHGSat from 2022 to 2024. Both platforms find emission maxima in the first quarter (JFM) and minima in the third quarter (JAS). Insight M emissions were on average roughly 50% higher in JFM than JAS. GHGSat emissions were also on average 50% higher in JFM than JAS, and 30% higher in winter (DJF) than summer (JJA). These fluctuations are smaller than but consistent with the 60% fluctuation in total emissions we infer from TROPOMI.

### **3.3 Drivers of Permian emission seasonality**

Understanding what is driving the seasonal variability of Permian methane emissions could help identify mitigation opportunities. The economic predictors identified by Varon et al. (2023)<sup>15</sup> including gas price, new well development, flaring, and production cannot explain the seasonal variation. Rapid withdrawal of gas from underground storage facilities to meet winter heating demand could lead to higher throughput and emissions from combustion slip at compressor stations, but Permian storage volumes are too low (<80 Bcf in 2022<sup>43</sup>) for this to be a strong effect, and their seasonal cycle does not align with that of emissions<sup>17</sup>. Seasonal trends in equipment malfunction and maintenance events in the Permian are also an unlikely explanation, as those events are more frequently reported in summer than winter<sup>44,45</sup> (Figure S4). Winter highs in urban methane emissions have been attributed to increased gas consumption and post-meter leakage<sup>46,47</sup>, which could also occur in US oil and gas basins<sup>17</sup>, but the seasonal fluctuation in the Permian ( $\sim 2 \text{ Tg a}^{-1}$ ) is many times larger than observed in cities ( $\sim 50 \text{ Gg a}^{-1}$ ) despite a much lower population density. We hypothesize here that the winter maximum in Permian methane emissions could be driven by increased liquid storage tank emissions in cold conditions, caused by inadequate weatherization of wellhead separators.

In 2022, the Railroad Commission (RRC) of Texas introduced a new Weather Emergency Preparedness Standards rule requiring winter weatherization of critical natural gas facilities<sup>48</sup>. Hydrate formation and icing of control valves can occur in production, gathering, and transmission systems at freezing temperatures, and even above freezing<sup>49</sup>, due to the Joule-Thompson effect. RRC recommends using a combination of heating blankets, line heaters, catalytic heaters, and other solutions to prevent equipment from freezing in cold conditions<sup>50</sup>, but some Permian oil and gas infrastructure remains unweatherized<sup>51</sup>. Line and catalytic heaters, turned on in the fall and off in the spring and fueled by natural gas, could themselves represent a seasonal source of methane emissions. Festa-Bianchet et al. (2024)<sup>52</sup> found that catalytic heaters at upstream production facilities in British Columbia, Canada vented about 40% of incoming gas during winter operations, much higher than the standard assumption of 2% (98% efficiency) for combustion processes. The relatively small number of catalytic heaters in the Permian, however—at most 23,000 units (0.18 per well) in 2023 according to US Greenhouse Gas Reporting Program data for small combustion units<sup>53</sup>—cannot explain the 60% seasonal fluctuation we observe with TROPOMI.

The seasonal variability in Permian methane emissions may be more strongly driven by emissions from storage tanks for produced liquids, including water and liquid hydrocarbons. Emissions from these liquids could increase during the winter if they contain more dissolved gas under cold conditions, as one would expect from equilibrium thermodynamics (Henry's Law). Production facilities use separators to divide the well stream into its liquid and gaseous components. The liquids are stored in tanks at atmospheric pressure before being transported away by pipeline or truck, and the drop in pressure between separator and tank leads to the release of the dissolved gases in a process called “tank flashing”<sup>54,55</sup>. Poorly weatherized

separators operating at cold temperatures would send more dissolved gas to liquid storage tanks, which periodically vent when the tank pressure exceeds a near-atmospheric threshold. Cold weather could therefore lead to increased methane emissions from the storage of produced liquids across the basin.

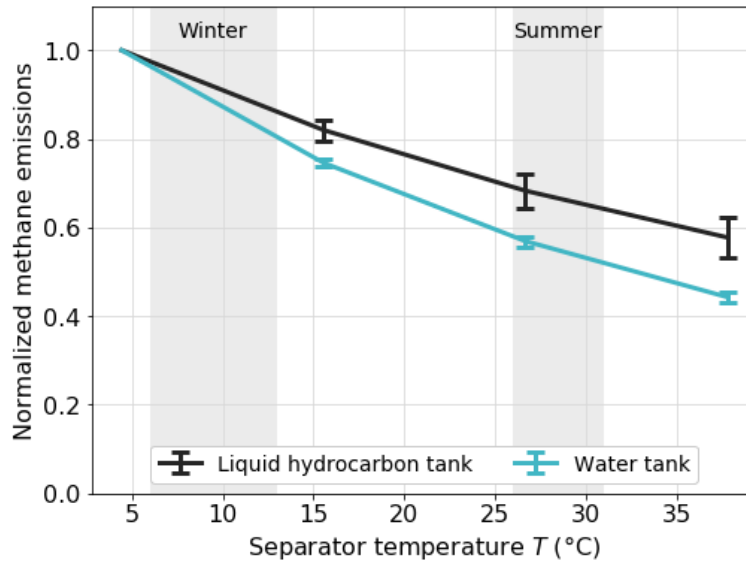


**Figure 5:** Tank flashing emissions from liquid hydrocarbon and water storage tanks for different separator temperatures  $T$ , normalized to emissions at  $T = 4.4^\circ\text{C}$  ( $40^\circ\text{F}$ ), based on thermodynamic simulations by Cardoso-Saldaña et al. (2021)<sup>56</sup>. The vertical bars represent the interquartile range of results for different combinations of separator pressure (20–1400 PSIA) and well stream composition (wide range of gas-to-oil ratios and liquid hydrocarbon densities). The shaded areas are ranges of monthly average surface temperatures for Midland, Texas in the winter and summer months from 2019 to 2023<sup>57</sup>.

To test this hypothesis, we analyzed thermodynamic simulations of separator efficiency and tank flashing emissions by Cardoso-Saldaña et al. (2021)<sup>56</sup> for different temperatures, pressures, and well stream compositions (wide range of gas-to-oil ratios and liquid hydrocarbon densities based on field measurements). The simulations are for a single-stage, unheated separator with water and liquid hydrocarbon tanks. Salt content and entrainment of hydrocarbon liquids into the water storage tank are not considered. Figure 5 plots the expected tank emissions at different ambient/separator temperatures. As expected, tank emissions decrease with

increasing temperature as the level of dissolved gas decreases. For example, emissions from liquid hydrocarbon tanks are 39%–55% higher at 4°C than at 27°C and emissions from water tanks are 72%–79% higher.

Monthly average surface temperature in Midland, Texas ranged from 26°C to 31°C during the summer months and 6°C to 13°C during the winter months from 2019 to 2023<sup>57</sup>. We see from Figure 5 that ~50% higher tank flashing emissions in winter are plausible. Liquid storage tanks accounted for 33% of total emissions detected in a September–November 2019 aerial survey of 1100 Permian methane point sources by Cusworth et al. (2021)<sup>9</sup> and a similar fraction of total emissions modeled by Sherwin et al. (2024)<sup>10</sup> for year-round surveys, in both cases the most of any source type. The temperature dependence of tank flashing emissions could thus explain much of the seasonal trend observed in the Permian.

### **3.4 Anadarko, Barnett, Eagle Ford, and Haynesville basins**

To determine whether the seasonal variation in emissions is unique to the Permian, we apply IMI continuous emission monitoring to four other south-central US oil and gas production regions: the Anadarko, Barnett, Eagle Ford, and Haynesville basins (Figure 1). These basins accounted for 11% (25%) of US oil (gas) production in 2023<sup>37</sup> and have been identified as high emitters in previous analyses of satellite observations<sup>14,58</sup>. We perform weekly regional inversions for each basin over two years from 2022 to 2023 and report total methane emissions and intensities. Our inversions assume normal error statistics on emissions and begin in July 2021, but as for the Permian we discard the first six months of results as a burn-in period.

Figure 6 shows the resulting oil and gas methane emission estimates for the four basins as annual and 12-week moving averages, along with time series for gas production, methane

intensity, and active well count. Mean 2022–2023 emissions average  $0.76 \text{ Tg a}^{-1}$  for the Anadarko,  $0.46 \text{ Tg a}^{-1}$  for Eagle Ford,  $0.46 \text{ Tg a}^{-1}$  for Haynesville, and  $0.40 \text{ Tg a}^{-1}$  for the Barnett. These values are similar to those reported by Shen et al. (2022)<sup>58</sup> based on analysis of TROPOMI observations for 2018–2020. Seasonal trends are not as strong as those observed in the Permian, but they are broadly consistent; the Anadarko, Barnett, and Haynesville basins all show local emission minima in the summer or fall and maxima in the winter or spring. Differences in seasonal variations (such as for the Eagle Ford) may reflect different seasonal conditions and practices, or simply the shorter study period.

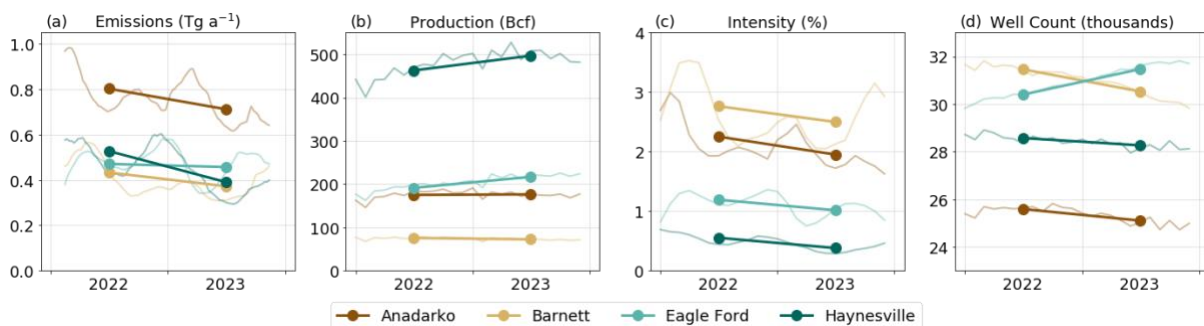


**Figure 6:** (a) Methane emissions, (b) gas production, (c) methane intensity, and (d) active well counts in the US Anadarko, Barnett, Eagle Ford, and Haynesville basins, from 2022 to 2023. Data for gas production and well counts are from Enverus Drillinginfo<sup>37</sup>. Thick dark lines show annual averages. Thin light lines show (a) 12-week moving average emissions, (b) monthly average gas production, (c) 3-month moving average methane intensity computed as in Figure 2 but assuming 90% methane gas content<sup>59</sup>, and (d) monthly average well count.

The methane intensities in Figure 6 are computed here as in Figure 2, but assuming 90% methane gas content for all four basins<sup>59</sup>. Average methane intensity was 2.1% in the Anadarko, 2.6% in the Barnett, 1.1% in Eagle Ford, and 0.5% in Haynesville. These intensities are a factor of 2–3 lower than estimated by Lu et al. (2023)<sup>14</sup> for the years 2010–2019 based on GOSAT satellite observations, except for the Barnett, where we both estimate 2.6% intensity. The higher intensity in the Barnett despite its relatively low emissions likely reflects low and declining production<sup>60</sup>. The Haynesville’s much lower intensity likely reflects more efficient practices in

the primarily gas-producing basin. Intensity declined in all basins from 2022 to 2023, reflecting decreasing emissions and increasing production everywhere except the Barnett, which saw declines in both. Annual intensity decreased by 0.30% in the Anadarko (i.e., from 2.25% to 1.95%), 0.27% in the Barnett, 0.18% in Eagle Ford, and 0.17% in Haynesville.

In summary, five years of weekly TROPOMI methane inversions for the Permian basin (2019–2023) reveal declining methane intensity and strong seasonal variability in total emissions, 60% higher in winter than summer. The decreasing intensity is driven by increasing production, not decreasing emissions, and the seasonality is corroborated by independent tower, aerial, and facility-level satellite observations. Two years (2022–2023) of weekly inversions for the nearby Anadarko, Barnett, Eagle Ford, and Haynesville basins reveal similar seasonal fluctuations and declining intensity. The winter maximum may be driven in large part by higher emissions from the storage of produced liquids due to decreased separator efficiency in cold conditions. Better weatherization of facilities could significantly decrease emissions.

### **Supporting Information**

Additional description of Insight M and GHGSat emission analysis (Text S1, S2; Fig. S1) and additional figures for TX/NM emission estimates (Fig. S2), GHGSat plume detections (Fig. S3), and TX/NM excess emission reporting data (Fig. S4).

### **Corresponding Author**

\*Daniel J. Varon (danielvaron@g.harvard.edu)

### **Author Contributions**

DJV and DJJ designed the study. DJV performed the satellite inverse analysis and wrote the first draft of the manuscript. ZB performed the tower inverse analysis. EDS and HK performed the Insight M emission analysis. DJ performed the GHGSat emission analysis. FCS analyzed the thermodynamic simulations of separator efficiency. All authors contributed to the interpretation of results and writing the manuscript.

### **Acknowledgements**

This work was supported by the Harvard Initiative on Reducing Global Methane Emissions, the National Aeronautics and Space Administration (NASA) Carbon Monitoring System, the NASA Jet Propulsion Laboratory initiative for the US GHG Center, Environmental Defense Fund, GHGSat Inc., and ExxonMobil Technology and Engineering Company. Part of this research was carried out at the Jet Propulsion Laboratory, California Institute of Technology, under contract with NASA (80NM0018D0004). This work was partially supported by the California Energy Commission (SUMMATION project, agreement number PIR-17-015). It does not necessarily represent the views of the Energy Commission, its employees, or the State of California. The Energy Commission, the State of California, its employees, contractors, and subcontractors make

no warranty, express or implied, and assume no legal liability for the information in this report; nor does any party represent that the uses of this information will not infringe upon privately owned rights. This paper has not been approved or disapproved by the California Energy Commission, nor has the California Energy Commission passed upon the accuracy or adequacy of the information in this paper. This manuscript has been authored by authors at Lawrence Berkeley National Laboratory under Contract No. DE-AC02-05CH11231 with the U.S. Department of Energy. The U.S. Government retains, and the publisher, by accepting the article for publication, acknowledges, that the U.S. Government retains a non-exclusive, paid-up, irrevocable, world-wide license to publish or reproduce the published form of this manuscript, or allow others to do so, for U.S. Government purposes.

## References

1. Jacob, D. J., Turner, A. J., Maasakkers, J. D., Sheng, J., Sun, K., Liu, X., Chance, K., Aben, I., McKeever, J., and Frankenberg, C.: Satellite observations of atmospheric methane and their value for quantifying methane emissions, *Atmos. Chem. Phys.*, 16, 14371–14396, <https://doi.org/10.5194/acp-16-14371-2016>, 2016.
2. Jacob, D. J., Varon, D. J., Cusworth, D. H., Dennison, P. E., Frankenberg, C., Gautam, R., Guanter, L., Kelley, J., McKeever, J., Ott, L. E., Poulter, B., Qu, Z., Thorpe, A. K., Worden, J. R., and Duren, R. M.: Quantifying methane emissions from the global scale down to point sources using satellite observations of atmospheric methane, *Atmos. Chem. Phys.*, 22, 9617–9646, <https://doi.org/10.5194/acp-22-9617-2022>, 2022.
3. Veefkind, J. P., Aben, I., McMullan, K., Förster, H., De Vries, J., Otter, G., Claas, J., Eskes, H.J., De Haan, J.F., Kleipool, Q., and Van Weele, M.: TROPOMI on the ESA

Sentinel-5 Precursor: A GMES mission for global observations of the atmospheric composition for climate, air quality and ozone layer applications, *Remote Sens. Environ.*, 120, 70–83, <https://doi.org/10.1016/j.rse.2011.09.027>, 2012.

*Environ.*, 120, 70–83, <https://doi.org/10.1016/j.rse.2011.09.027>, 2012.

4. Lorente, A., Borsdorff, T., Butz, A., Hasekamp, O., aan de Brugh, J., Schneider, A., Wu, L., Hase, F., Kivi, R., Wunch, D., Pollard, D. F., Shiomi, K., Deutscher, N. M., Velazco, V. A., Roehl, C. M., Wennberg, P. O., Warneke, T., and Landgraf, J.: Methane retrieved from TROPOMI: improvement of the data product and validation of the first 2 years of measurements, *Atmos. Meas. Tech.*, 14, 665–684, <https://doi.org/10.5194/amt-14-665-2021>, 2021.
5. Schneising, O., Buchwitz, M., Reuter, M., Vanselow, S., Bovensmann, H., and Burrows, J. P.: Remote sensing of methane leakage from natural gas and petroleum systems revisited, *Atmos. Chem. Phys.*, 20, 9169–9182, <https://doi.org/10.5194/acp-20-9169-2020>, 2020.
6. Federal Reserve Bank of Dallas (FRBD): Energy in the Eleventh District: Permian Basin: Oil production, <https://www.dallasfed.org/research/energy11/permian.aspx#Oil>, last access: 21 April 2025.
7. Zhang, Y., Gautam, R., Pandey, S., Omara, M., Maasackers, J. D., Sadavarte, P., Lyon, D., Nesser, H., Sulprizio, M. P., Varon, D. J., Zhang, R., Houweling, S., Zavala-Araiza, D., Alvarez, R. A., Lorente, A., Hamburg, S. P., Aben, I., and Jacob, D. J.: Quantifying methane emissions from the largest oil-producing basin in the United States from space, *Sci. Adv.*, 6, 17, <https://doi.org/10.1126/sciadv.aaz5120>, 2020.

8. Irakulis-Loitxate, I., Guanter, L., Liu, Y.-N., Varon, D. J., Maasakkers, J. D., Zhang, Y., Thorpe, A. K., Duren, R. M., Frankenberg, C., Lyon, D., Hmiel, B., Cusworth, D. H., Zhang, Y., Segl, K., Gorrion, J., Sanchez-García, E., Sulprizio, M. P., Cao, K., Zhu, H., Liang, J., Li, X., Aben, I., and Jacob, D. J.: Satellite-based survey of extreme methane emissions in the Permian Basin , *Sci. Adv.*, 7, eabf4507, <https://doi.org/10.1126/sciadv.abf4507>, 2021.
9. Cusworth, D. H., Duren, R. M., Thorpe, A. K., Olson-Duvall, W., Heckler, J., Chapman, J. W., Eastwood, M. L., Helmlinger, M. C., Green, R. O., Asner, G. P., Dennison, P. E., and Miller, C. E.: Intermittency of large methane emitters in the Permian Basin, *Environ. Sci. Tech. Lett.*, 8, 567–573, <https://doi.org/10.1021/acs.estlett.1c00173>, 2021.
10. Sherwin, E. D., Rutherford, J. S., Zhang, Z., Chen, Y., Wetherley, E. B., Yakovlev, P. V., Berman, E. S. F., Jones, B. B., Cusworth, D. H., Thorpe, A. K., Ayasse, A. K., Duren, R. M., and Brandt, A. R.: US oil and gas system emissions from nearly one million aerial site measurements, *Nature* 627, 328–334, <https://doi.org/10.1038/s41586-024-07117-5>, 2024.
11. Barkley, Z., Davis, K., Miles, N., Richardson, S., Deng, A., Hmiel, B., Lyon, D., and Lauvaux, T.: Quantification of oil and gas methane emissions in the Delaware and Marcellus basins using a network of continuous tower-based measurements, *Atmos. Chem. Phys.*, 23, 6127–6144, <https://doi.org/10.5194/acp-23-6127-2023>, 2023.

12. OGCi: Methane Intensity Target, <https://www.ogci.com/action-and-engagement/reducing-methane-emissions/#methane-target>, (last access: 21 April 2025), 2024.
13. Chen, Y., Sherwin, E. D., Berman, E. S. F., Jones, B. B., Gordon, M. P., Wetherley, E. B., Kort, E. A., and Brandt, A. R.: Quantifying Regional Methane Emissions in the New Mexico Permian Basin with a Comprehensive Aerial Survey, *Environ. Sci. Technol.*, 56, 4317–4323, <https://doi.org/10.1021/acs.est.1c06458>, 2022.
14. Lu, X., Jacob, D. J., Zhang, Y., Shen, L., Sulprizio, M. P., Maasakkers, J. D., Varon, D. J., Qu, Z., Chen, Z., Hmiel, B., Parker, R. J., Boesch, H., Wang, H., He, C., and Fan, S.: Observation-derived 2010–2019 trends in methane emissions and intensities from US oil and gas fields tied to activity metrics, *P. Natl. Acad. Sci. USA*, 120, e2217900120, <https://doi.org/10.1073/pnas.2217900120>, 2023.
15. Varon, D. J., Jacob, D. J., Hmiel, B., Gautam, R., Lyon, D. R., Omara, M., Sulprizio, M., Shen, L., Pendergrass, D., Nesser, H., Qu, Z., Barkley, Z. R., Miles, N. L., Richardson, S. J., Davis, K. J., Pandey, S., Lu, X., Lorente, A., Borsdorff, T., Maasakkers, J. D., and Aben, I.: Continuous weekly monitoring of methane emissions from the Permian Basin by inversion of TROPOMI satellite observations, *Atmos. Chem. Phys.*, 23, 7503–7520, <https://doi.org/10.5194/acp-23-7503-2023>, 2023.
16. Vanselow, S., Schneising, O., Buchwitz, M., Reuter, M., Bovensmann, H., Boesch, H., and Burrows, J. P.: Automated detection of regions with persistently enhanced methane concentrations using Sentinel-5 Precursor satellite data, *Atmos. Chem. Phys.*, 24, 10441–10473, <https://doi.org/10.5194/acp-24-10441-2024>, 2024.

17. Hu, L., Andrews, A. E., Montzka, S. A., Miller, S. M., Bruhwiler, L., Oh, Y., Sweeney, C., Miller, J. B., McKain, K., Ibarra Espinosa, S. Davis, K., Miles, N., Mountain, M., Lan, X., Crotwell, A., Madronich, M., Mefford, T., Michel, S., and Houwelling, S.: An Unexpected Seasonal Cycle in U.S. Oil and Gas Methane Emissions, *Environmental Science & Technology*, DOI: 10.1021/acs.est.4c14090, 2025.
18. Varon, D. J., Jacob, D. J., Sulprizio, M., Estrada, L. A., Downs, W. B., Shen, L., Hancock, S. E., Nesser, H., Qu, Z., Penn, E., Chen, Z., Lu, X., Lorente, A., Tewari, A., and Randles, C. A.: Integrated Methane Inversion (IMI 1.0): a user-friendly, cloud-based facility for inferring high-resolution methane emissions from TROPOMI satellite observations, *Geosci. Model Dev.*, 15, 5787–5805, <https://doi.org/10.5194/gmd-15-5787-2022>, 2022.
19. Estrada, L. A., Varon, D. J., Sulprizio, M., Nesser, H., Chen, Z., Balasus, N., Hancock, S. E., He, M., East, J. D., Mooring, T. A., Oort Alonso, A., Maasakkers, J. D., Aben, I., Baray, S., Bowman, K. W., Worden, J. R., Cardoso-Saldaña, F. J., Reidy, E., and Jacob, D. J.: Integrated Methane Inversion (IMI) 2.0: an improved research and stakeholder tool for monitoring total methane emissions with high resolution worldwide using TROPOMI satellite observations, *EGUsphere* [preprint], <https://doi.org/10.5194/egusphere-2024-2700>, 2025.
20. Balasus, N., Jacob, D. J., Lorente, A., Maasakkers, J. D., Parker, R. J., Boesch, H., Chen, Z., Kelp, M. M., Nesser, H., and Varon, D. J.: A blended TROPOMI+GOSAT satellite data product for atmospheric methane using machine learning to correct

retrieval biases, *Atmos. Meas. Tech.*, 16, 3787–3807, <https://doi.org/10.5194/amt-16-3787-2023>, 2023.

21. Borsdorff, T., Martinez-Velarte, M. C., Sneep, M., ter Linden, M., and Landgraf, J.: Random Forest Classifier for Cloud Clearing of the Operational TROPOMI XCH<sub>4</sub> Product., *Remote Sensing* 16, 1208, 2024.
22. Maasakkers, J. D., McDuffie, E. E., Sulprizio, M. P., Chen, C., Schultz, M., Brunelle, L., Thrush, R., Steller, J., Sherry, C., Jacob, D. J., Jeong, S., Irving, B., and Weitz, M.: A Gridded Inventory of Annual 2012–2018 U.S. Anthropogenic Methane Emissions, *Environ. Sci. Technol.*, 57, 16276–16288, <https://doi.org/10.1021/acs.est.3c05138>, 2023.
23. Bloom, A. A., Bowman, K. W., Lee, M., Turner, A. J., Schroeder, R., Worden, J. R., Weidner, R. J., McDonald, K. C., and Jacob, D. J.: CMS: Global 0.5-deg Wetland Methane Emissions and Uncertainty (WetCHARTs v1.3.1), ORNL DAAC, <https://doi.org/10.3334/ORNLDAAC/1915>, 2021.
24. GEOS-Chem Classic (GCCClassic) version 14.2.3, available at [10.5281/zenodo.10246625](https://zenodo.org/record/10246625), 2023.
25. Randerson, J. T., Van Der Werf, G. R., Giglio, L., Collatz, G. J., and Kasibhatla, P. S.: Global Fire Emissions Database, Version 4.1 (GFEDv4), ORNL DAAC, <https://doi.org/10.3334/ORNLDAAC/1293>, 2017.

26. Etiope, G., Ciotoli, G., Schwietzke, S., and Schoell, M.: Gridded maps of geological methane emissions and their isotopic signature, *Earth System Science Data*, 11, 1–22, <https://doi.org/10.5194/essd-11-1-2019>, 2019.
27. Hmiel, B., Petrenko, V. V., Dyonisius, M. N., Buizert, C., Smith, A. M., Place, P. F., Harth, C., Beaudette, R., Hua, Q., Yang, B., Vimont, I., Michel, S. E., Severinghaus, J. P., Etheridge, D., Bromley, T., Schmitt, J., Fäin, X., Weiss, R. F., and Dlugokencky, E.: Preindustrial  $^{14}\text{CH}_4$  indicates greater anthropogenic fossil  $\text{CH}_4$  emissions, *Nature*, 578, 409–412, <https://doi.org/10.1038/s41586-020-1991-8>, 2020.
28. Fung, I., John, J., Lerner, J., Matthews, E., Prather, M., Steele, L. P., and Fraser, P. J.: Three-dimensional model synthesis of the global methane cycle, *Journal of Geophysical Research: Atmospheres*, 96, 13033–13065, <https://doi.org/10.1029/91JD01247>, 1991.
29. Murguia-Flores, F., Arndt, S., Ganesan, A. L., Murray-Tortarolo, G., and Hornibrook, E. R. C.: Soil Methanotrophy Model (MeMo v1.0): a process-based model to quantify global uptake of atmospheric methane by soil, *Geosci. Model Dev.*, 11, 2009–2032, <https://doi.org/10.5194/gmd-11-2009-2018>, 2018.
30. Shen, L., Zavala-Araiza, D., Gautam, R., Omara, M., Scarpelli, T., Sheng, J., Sulprizio, M. P., Zhuang, J., Zhang, Y., Lu, X., Hamburg, S. P., and Jacob, D. J.: Unravelling a large methane emission discrepancy in Mexico using satellite observations, *Remote Sens. Environ.*, 260, 112461, <https://doi.org/10.1016/j.rse.2021.112461>, 2021.

31. Brasseur, G. P. and Jacob, D. J.: Modeling of Atmospheric Chemistry, Cambridge University Press, Cambridge, UK, <https://doi.org/10.1017/9781316544754>, 2017.
32. Chen, Z., Jacob, D. J., Gautam, R., Omara, M., Stavins, R. N., Stowe, R. C., Nesser, H., Sulprizio, M. P., Lorente, A., Varon, D. J., Lu, X., Shen, L., Qu, Z., Pendergrass, D. C., and Hancock, S.: Satellite quantification of methane emissions and oil–gas methane intensities from individual countries in the Middle East and North Africa: implications for climate action, *Atmos. Chem. Phys.*, 23, 5945–5967, <https://doi.org/10.5194/acp-23-5945-2023>, 2023.
33. Maasackers, J. D., Jacob, D. J., Sulprizio, M. P., Scarpelli, T. R., Nesser, H., Sheng, J.-X., Zhang, Y., Hersher, M., Bloom, A. A., Bowman, K. W., Worden, J. R., Janssens-Maenhout, G., and Parker, R. J.: Global distribution of methane emissions, emission trends, and OH concentrations and trends inferred from an inversion of GOSAT satellite data for 2010–2015, *Atmos. Chem. Phys.*, 19, 7859–7881, <https://doi.org/10.5194/acp-19-7859-2019>, 2019.
34. Rodgers, C. D.: Inverse Methods for Atmospheric Sounding: Theory and Practice, World Scientific, River Edge, USA, ISBN 978-9810227401, 2000.
35. Hancock, S. E., Jacob, D. J., Chen, Z., Nesser, H., Davitt, A., Varon, D. J., Sulprizio, M. P., Balasus, N., Estrada, L. A., Cazorla, M., Dawidowski, L., Diez, S., East, J. D., Penn, E., Randles, C. A., Worden, J., Aben, I., Parker, R. J., and Maasackers, J. D.: Satellite quantification of methane emissions from South American countries: a high-resolution inversion of TROPOMI and GOSAT observations, *Atmos. Chem. Phys.*, 25, 797–817, <https://doi.org/10.5194/acp-25-797-2025>, 2025.

36. Lyon, D. R., Hmiel, B., Gautam, R., Omara, M., Roberts, K. A., Barkley, Z. R., Davis, K. J., Miles, N. L., Monteiro, V. C., Richardson, S. J., Conley, S., Smith, M. L., Jacob, D. J., Shen, L., Varon, D. J., Deng, A., Rudelis, X., Sharma, N., Story, K. T., Brandt, A. R., Kang, M., Kort, E. A., Marchese, A. J., and Hamburg, S. P.: Concurrent variation in oil and gas methane emissions and oil price during the COVID-19 pandemic, *Atmos. Chem. Phys.*, 21, 6605–6626, <https://doi.org/10.5194/acp-21-6605-2021>, 2021.
37. Enverus: Drillinginfo, <https://app.drillinginfo.com/production>, last access: 23 April 2025.
38. New Mexico Administrative Code (NMAC): N.M. Admin. Code § 19.15.27.9 - STATEWIDE NATURAL GAS CAPTURE REQUIREMENTS, <https://www.srca.nm.gov/parts/title19/19.015.0027.html>, 2021.
39. New Mexico Administrative Code (NMAC): N.M. Admin. Code § 20.2.50 - OZONE PRECURSOR POLLUTANTS, <https://www.env.nm.gov/wp-content/uploads/sites/2/2022/07/Oil-and-Gas-Sector-Ozone-Precursor-Polutants-Final-rule-20.2.50-NMAC-06Jul22.pdf>, 2022.
40. Monteiro, V. C., Miles, N. L., Richardson, S. J., Barkley, Z., Haupt, B. J., Lyon, D., Hmiel, B., and Davis, K. J.: Methane, carbon dioxide, hydrogen sulfide, and isotopic ratios of methane observations from the Permian Basin tower network, *Earth Syst. Sci. Data*, 14, 2401–2417, <https://doi.org/10.5194/essd-14-2401-2022>, 2022.
41. Sherwin, E., Kruguer, J., Wetherley, E. B., Yakovlev, P. V., Brandt, A., Deiker, S., Berman, E. S. F., and Biraud, S.: Comprehensive Aerial Surveys Find a Reduction in

Permian Basin Methane Intensity from 2020-2023, [preprint]

<https://dx.doi.org/10.2139/ssrn.5087216>, 2025.

42. Jervis, D. et al.: Contribution of Large Point-Sources to 2023 Global Energy Sector Methane Emissions, in review, 2025.
43. East Daley Analytics (EDA): Where is Excess Permian Supply Going? Available at <https://www.eastdaley.com/media-and-news/where-is-excess-permian-supply-going>, last access: 21 May 2025.
44. Texas Commission on Environmental Quality (TCEQ): Air Emissions and Maintenance Events, available at: <https://www.tceq.texas.gov/airquality/emission-events>, 2025, last access: 21 April 2025.
45. New Mexico Environment Department (NMED): Excess Emission Reports, available at: <https://www.env.nm.gov/air-quality/compliance-and-enforcement/>, 2025, last access: 21 April 2025.
46. Sargent, M. R., Floerchinger, C., McKain, K., Budney, J., Gottlieb, E. W., Hutyra, L. R., Rudek, J., and Wofsy, S. C.: Majority of US urban natural gas emissions unaccounted for in inventories, *P. Natl. Acad. Sci. USA*, 118, e2105804118, <https://doi.org/10.1073/pnas.2105804118>, 2021.
47. Karion, A., Ghosh, S., Lopez-Coto, I., Mueller, K., Gourdji, S., Pitt, J., and Whetstone, J.: Methane Emissions Show Recent Decline but Strong Seasonality in Two US Northeastern Cities, *Environ. Sci. Technol.*, 57, 19565–19574, <https://doi.org/10.1021/acs.est.3c05050>, 2023.

48. Texas Register (TR): Title 16, Part 1, Chapter 3, Rule §3.66 - WEATHER EMERGENCY PREPAREDNESS STANDARDS, [https://sos.appianportalsgov.com/rules-and-meetings?interface=VIEW\\_TEXAS\\_REGISTER\\_SUMMARY&recordId=409724](https://sos.appianportalsgov.com/rules-and-meetings?interface=VIEW_TEXAS_REGISTER_SUMMARY&recordId=409724), 2022.
49. Liu, Z., Zerpa, L. E., and Wang, Y.: Hydrate Problems for Gas Lift Operations for Deepwater and Arctic Wells and Best Practices for Prevention, Paper presented at the SPE Western Regional Meeting, Anchorage, Alaska, USA, May 2016. doi: <https://doi.org/10.2118/180392-MS>, 2016.
50. Railroad Commission of Texas (RRC): RRC Weatherization Practices Guidance Document –Gas Supply Chain Facilities and Pipeline Facilities, <https://www.rrc.texas.gov/media/voxi53y/rrc-weatherization-practices-and-recommendations-report.pdf>, 2024, last access: 21 April 2025.
51. US Energy Information Administration (EIA): Winter storms have disrupted U.S. natural gas production, <https://www.eia.gov/todayinenergy/detail.php?id=61563#:~:text=Some%20natural%20gas%20infrastructure%20in%20the%20Permian%20is,by%20almost%205%20Bcf%2Fd%20in%20that%20region%20alone>, 2024a, last access: 21 April 2025.
52. Festa-Bianchet, S. A., Mohammadikharkeshi, M., Tyner, D. R., and Johnson, M. R.: Catalytic Heaters at Oil and Gas Sites May be a Significant yet Overlooked Seasonal Source of Methane Emissions, *Environ. Sci. Tech. Lett.*, 11, 9,

<https://doi.org/10.1021/acs.estlett.4c00453?urlappend=%3Fref%3DPDF&jav=VoR&rel=cite-as>, 2024.

53. Environmental Protection Agency (EPA): Envirofacts Database Greenhouse Gas Query Builder, available at <https://enviro.epa.gov/query-builder/ghg>, last access: 26 January 2025.
54. Allen, D. T., Cardoso-Saldaña, F. J., Kimura, Y., Chen, Q., Xiang, Z., Zimmerle, D., Bell, C., Lute, C., Duggan, J., and Harrison, M.: A Methane Emission Estimation Tool (MEET) for predictions of emissions from upstream oil and gas well sites with fine scale temporal and spatial resolution: Model structure and applications, *Sci. Total Environ.*, 829, 154277, <https://doi.org/10.1016/j.scitotenv.2022.154277>, 2022.
55. Caulton, D. R., Gurav, P. D., Robertson, A. M., Pozsonyi, K., Murphy, S. M., and Lyon, D. R.: Abnormal tank emissions in the Permian Basin identified using ethane to methane ratios. *Elem. Sci. Anthr.* 11 (1), 00121, DOI: 10.1525/elementa.2022.00121, 2023.
56. Cardoso-Saldaña, F.J., Pierce, K., Chen, Q., Kimura, Y., and Allen, D. T.: A searchable database for prediction of emission compositions from upstream oil and gas sources, *Environ. Sci. Technol.*, 55, pp. 3210-3218, <https://dx.doi.org/10.1021/acs.est.0c05925?ref=pdf>, 2021.
57. NOAA National Weather Service (NWS): NOWData, available at <https://www.weather.gov/wrh/Climate?wfo=maf>, 2025, last access: 21 April 2025.

58. Shen, L., Gautam, R., Omara, M., Zavala-Araiza, D., Maasackers, J. D., Scarpelli, T. R., Lorente, A., Lyon, D., Sheng, J., Varon, D. J., Nesser, H., Qu, Z., Lu, X., Sulprizio, M. P., Hamburg, S. P., and Jacob, D. J.: Satellite quantification of oil and natural gas methane emissions in the US and Canada including contributions from individual basins, *Atmos. Chem. Phys.*, 22, 11203–11215, <https://doi.org/10.5194/acp-22-11203-2022>, 2022.
59. Alvarez, R. A., Zavala-Araiza, D., Lyon, D. R., Allen, D. T., Barkley, Z. R., Brandt, A. R., Davis, K. J., Herndon, S. C., Jacob, D. J., Karion, A., Kort, E. A., Lamb, B. K., Lauvaux, T., Maasackers, J. D., Marchese, A. J., Omara, M., Pacala, S. W., Peischl, J., Robinson, A. L., Shepson, P. B., Sweeney, C., Townsend-Small, A., Wofsy, S. C., and Hamburg, S. P.: Assessment of methane emissions from the U.S. oil and gas supply chain, *Science*, 361, 186–188, <https://doi.org/10.1126/science.aar7204>, 2018.
60. Omara, M., Zavala-Araiza, D., Lyon, D. R., Hmiel, B., Roberts, K. A., and Hamburg, S. P.: Methane emissions from US low production oil and natural gas well sites, *Nat. Commun.*, 13, 2085, <https://doi.org/10.1038/s41467-022-29709-3>, 2022.

# *Supporting information: Seasonality and declining intensity of methane emissions from the Permian and nearby US oil and gas basins*

*Daniel J. Varon<sup>1</sup> ([danielvaron@g.harvard.edu](mailto:danielvaron@g.harvard.edu)), Daniel J. Jacob<sup>1</sup>, Lucas A. Estrada<sup>1</sup>, Nicholas Balasus<sup>1</sup>, James D. East<sup>1</sup>, Drew C. Pendergrass<sup>1</sup>, Zichong Chen<sup>1</sup>, Melissa Sulprizio<sup>1</sup>, Mark Omara<sup>2</sup>, Ritesh Gautam<sup>2</sup>, Zachary R. Barkley<sup>3</sup>, Felipe J. Cardoso-Saldaña<sup>4</sup>, Emily K. Reidy<sup>4</sup>, Harshil Kamdar<sup>5,6</sup>, Evan D. Sherwin<sup>7</sup>, Sebastien C. Biraud<sup>7</sup>, Dylan Jervis<sup>8</sup>, Sudhanshu Pandey<sup>9</sup>, John R. Worden<sup>9</sup>, Kevin W. Bowman<sup>9</sup>, Joannes D. Maasakkers<sup>10</sup>, Robert L. Kleinberg<sup>11</sup>*

<sup>1</sup> Harvard University, School of Engineering and Applied Science

<sup>2</sup> Environmental Defense Fund

<sup>3</sup> The Pennsylvania State University, Department of Meteorology and Atmospheric Science

<sup>4</sup> ExxonMobil Technology and Engineering Company

<sup>5</sup> Insight M

<sup>6</sup> Harvard University, Salata Institute for Climate and Sustainability

<sup>7</sup> Lawrence Berkeley National Laboratory

<sup>8</sup> GHGSat, Inc.

<sup>9</sup> Jet Propulsion Laboratory, California Institute of Technology

<sup>10</sup> Space Research Organisation Netherlands (SRON)

<sup>11</sup> Columbia University Center on Global Energy Policy

Keywords: Permian, methane, seasonality, TROPOMI

**Text S1: Insight M aerial surveys**

Insight M deploys an infrared spectrometer system that identifies the presence of methane through its differential absorption of specific frequencies of infrared in reflected sunlight. See Sherwin & Chen et al. 2021 for an independent characterization of the capabilities of the technology.

The fully anonymized Insight M data presented in this paper are drawn from commercial surveys conducted by Insight M in the Permian Basin from 2021–2023, documented in detail by Sherwin et al. (2025). These surveys encompass 47%–89% of natural gas production in the Permian basin, depending on the year, with similarly comprehensive coverage of midstream infrastructure such as pipelines, compressor stations, and natural gas processing plants.

To focus on seasonal patterns, we selected a subset of the full Permian dataset, including only assets that were measured at least once in each quarter of a given year. This substantially reduced both the overall coverage of the dataset, and often did so unevenly across asset types. Table S1 shows the comprehensiveness of asset coverage in each year, both for the full Permian survey and for the assets with quarterly coverage analyzed in this paper. Note that the subset of assets selected varies from year to year, as assets measured in every quarter in one year may not be measured in every quarter in another year.

**Table S1:** Fraction of Permian basin assets/production included in each year. Note that gathering and transmission pipelines were measured in all years at much higher rates than other asset types, a product of the commercial nature of data collection. Oil and natural gas production is computed for each well site on an annual average basis. Infrastructure location data are drawn from Enverus and Hart Energy & Mapping Data Services.

<b>Asset type</b>	<b>2021</b>	<b>2022</b>	<b>2023</b>
Well	1.0%	3.6%	9.0%
Compressor station	2.7%	6.4%	9.2%
Gas processing plant	2.8%	5.7%	10.6%
Gathering pipeline	20.3%	27.7%	39.1%
Transmission pipeline	35.6%	59.5%	60.9%
All pipelines	22.1%	34.8%	41.6%
Natural gas production	2.7%	4.6%	15.1%
Oil production	1.8%	3.0%	13.7%

We then computed total aerially detected emissions across all selected assets, without any estimate of emissions that were present but not detected by the Insight M aerial system, using the source-instantaneous Monte Carlo analysis method from Sherwin et al. (2024), described in greater detail in Appendix F of Sherwin et al. (2025). This method simulates emissions from each source (in this case 10,000 times), selecting a single emission rate from all measurements conducted at that source. Measurements that did not detect an emission are assigned an emission rate of 0 kg/hr.

We integrate quantification error using the approach from Sherwin et al. (2025), which assumes the quantification is unbiased on average (roughly consistent with the latest independent testing by El Abbadi et al. (2024), with a standard deviation of  $\pm 39\%$ , based on Sherwin & Chen et al. 2021. To enable year-to-year intercomparisons of observed seasonality, we normalize the resulting quarterly emissions estimates in each year, setting emissions in the first quarter equal to 1.

We then compute multi-year average seasonality results by conducting a weighted average of the above normalized results, weighting each quarter according to the number of source measurements conducted in that quarter. If the first quarter of 2021 included 1000 sources all measured once ( $1000 \times 1 = 1000$  measurements) and the first quarter of 2022 included 2000 sources all measured twice ( $2000 \times 2 = 4000$  measurements), then emissions from the first quarter of 2022 would have four times the weight of emissions from the first quarter of 2021. For simplicity, we apply the above weighted average approach to both mean values as well as 2.5<sup>th</sup> and 97.5<sup>th</sup> percentiles.

Note in Table S1 that pipelines are measured more comprehensively than other asset types. As a result, one must normalize emission by coverage completeness to gain insight into the relative share of total emissions contributed by different asset types in the surveyed region in each year. Figure S1 shows the estimated annual emissions breakdown in each year, both before and after adjusting for coverage completeness. For the assets included in this study, which were surveyed in each quarter of 2021, 2022, or 2023, the dominant emissions sources are well sites and compressor stations.

Well sites (simple, complex, and unspecified) contribute 36–57% of total measured emissions, and 31–67% after adjusting for coverage completeness. Compressor stations, range from 0.21–42% of total measured emissions and 0.23–59% after adjusting for coverage completeness. Pipelines, primarily gathering pipelines, represent a small share of total emissions, ranging from 1–2% of total measured emissions, falling to 0.1–0.6% after adjusting for coverage completeness. These results differ from the emissions breakdown in the full Permian, documented in Sherwin et al. (2025), in which gathering pipelines represent as much as 25% of the total in 2021.

This highlights the fact that the assets included in this study, those surveyed with quarterly frequency, are not representative of the full Permian basin. It is possible that seasonal trends in emissions may differ across sub-regions of the Permian basin. Answering such questions would require a representative or comprehensive aerial measurement dataset with quarterly resolution.

## **Text S2: GHGSat monitoring**

GHGSat operates a constellation of small satellites quantifying methane plumes at the facility scale based on high-resolution (25–30-m) retrievals of methane column enhancements over  $\sim 12 \times 15$  to  $12 \times 40$  km<sup>2</sup> targeted domains (Jervis et al., 2021). The GHGSat constellation grew from 5 instruments in 2022 to 10 in 2024, and four more are scheduled for launch in 2025.

In order to spatially attribute plumes detected on different days with estimated origin locations to common source locations, we perform a spatial aggregation procedure whereby any plume with an origin within a specified distance from another plume’s origin location is attributed to the same source location. We choose the aggregation distance to be 300m for plumes in the Permian basin from the O&G sector. The result is a cluster of  $M_i$  non-zero plumes  $\{q_i(t_j)\}$  that have been attributed to site  $i$ , detected at time  $t_j$ .

For every targeted GHGSat retrieval, we determine whether the retrieval footprint encompassed site  $i$ . If so, and no plume was detected, we count this as a null observation. The total number of observations of site  $i$ , including both plume detections and nulls, is then  $N_i$  with  $N_i \geq M_i$ .

The total number of site observations on day  $j$  is given by  $N(t_j) = \sum_i N_i(t_j)$ , the total plume emissions is given by  $Q(t_j) = \sum_i q_i(t_j)$ , and the total number of plume detections is given by  $M(t_j) = \sum_i m_i(t_j)$ , where  $m_i(t_j) = 1$  if  $q_i(t_j) \geq 0$  and  $m_i(t_j) = 0$  otherwise. We then convolve each of  $N(t_j)$ ,  $Q(t_j)$  and  $M(t_j)$  with a 45-day uniform running average to get the smoothed quantities  $\bar{N}(t_j)$ ,  $\bar{Q}(t_j)$ , and  $\bar{M}(t_j)$ .

The site-observation normalized emission rate and plume detections are then  $\bar{Q}(t_j)/\bar{N}(t_j)$  and  $\bar{M}(t_j)/\bar{N}(t_j)$ , respectively.

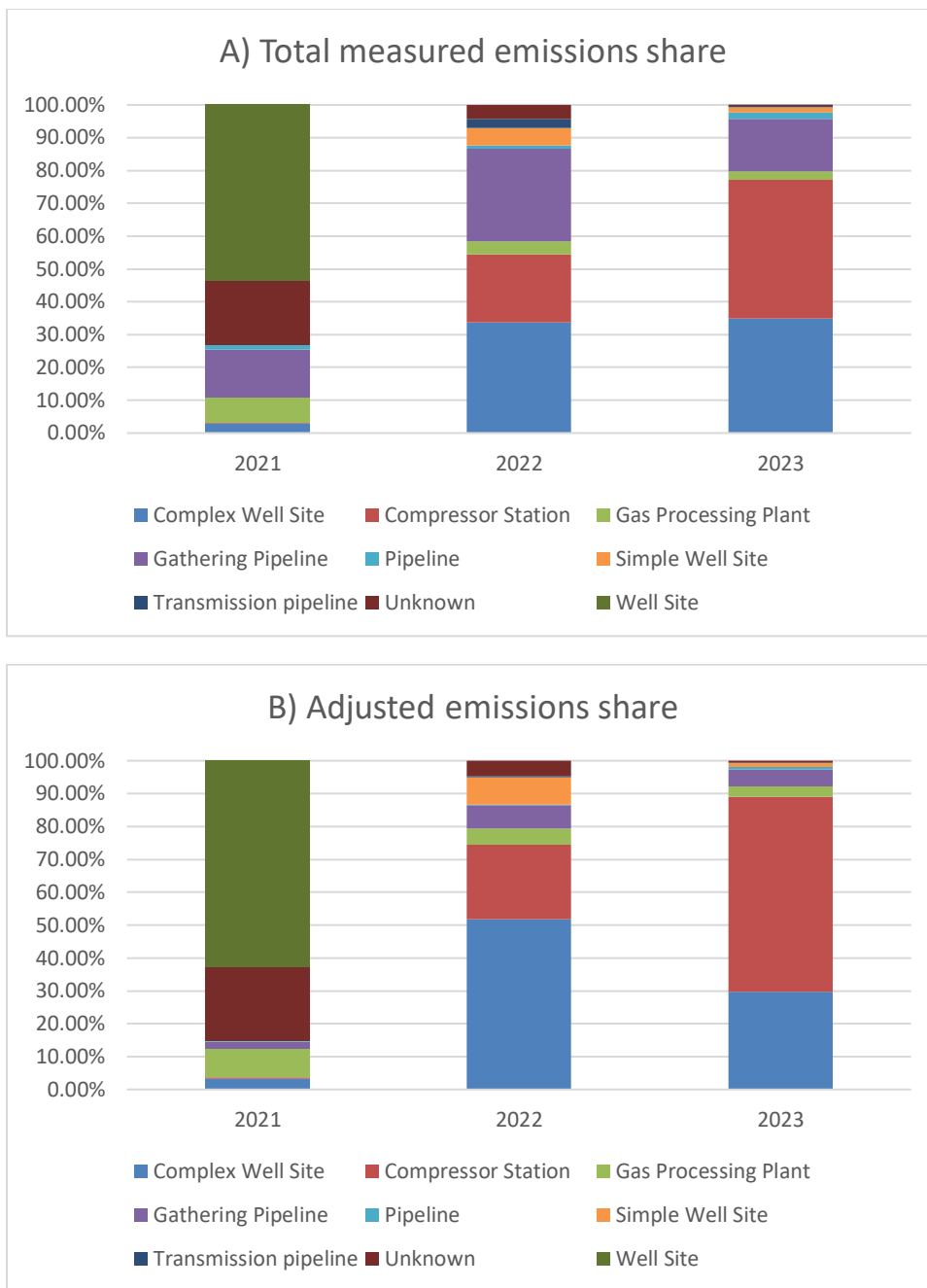
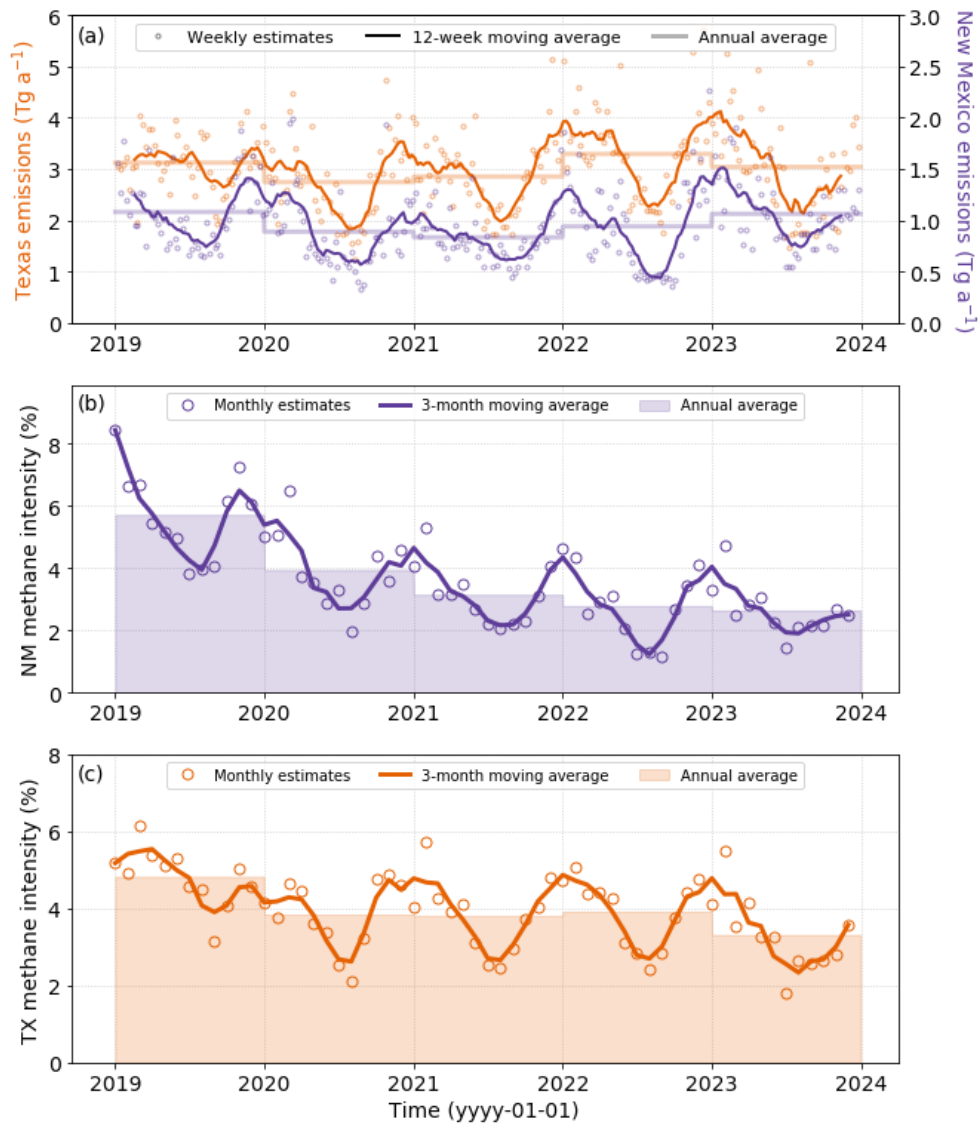
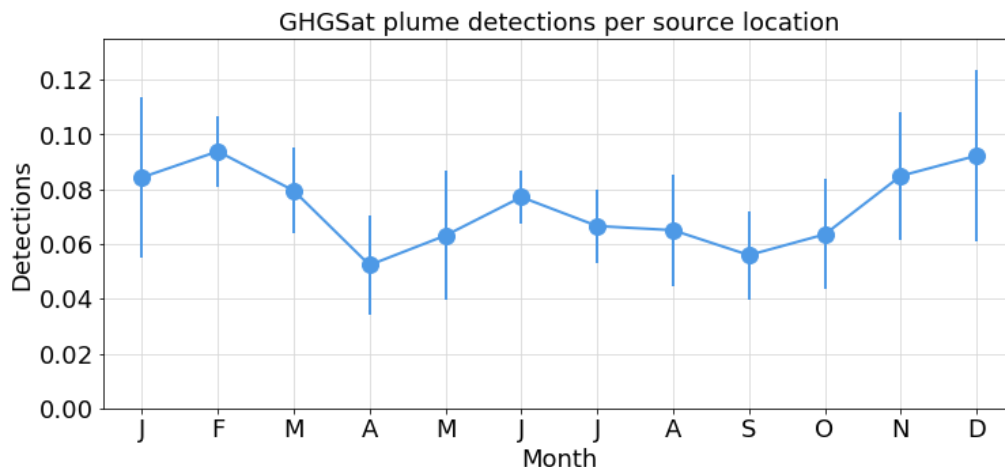


Figure S1. Emissions share by asset type for A) directly measured emissions and B) after adjusting for differences in coverage completeness across asset types.



**Figure S2:** Permian methane emissions and intensity by state from 2019 to 2023. (a) Total emissions from the Texas (orange) and New Mexico (purple) sections of the Permian Basin including weekly estimates, 12-week moving averages, and annual averages. The y-axis limits differ by a factor of 2. (b) Methane intensity in the New Mexico Permian from 2019 to 2023. (c) Methane intensity in the Texas Permian from 2019 to 2023. Monthly intensity values are computed as in Figure 2.



**Figure S3:** Monthly mean GHGSat plume detections per source location monitored in the Permian from 2022 to 2024. Error bars represent the standard deviations of daily values by month across years.

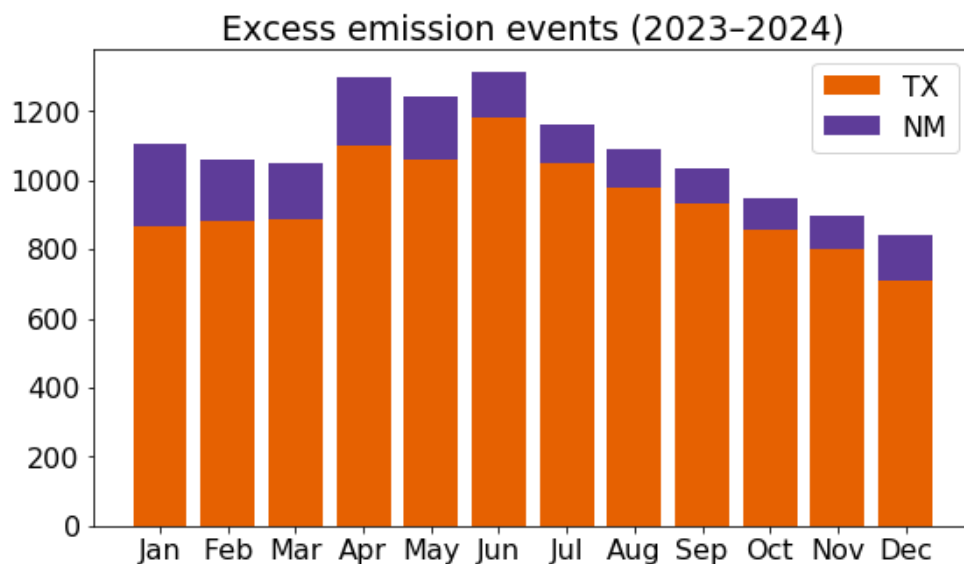


**Figure S4:** Total number of excess emission events for volatile organic compounds (VOCs) per month resulting from malfunction, maintenance, startup, and shutdown of oil and gas infrastructure in the New Mexico and Texas portions of the Permian Basin, as reported to the New Mexico Environment Department (NMED, 2025) and Texas Commission on Environmental Quality (TCEQ, 2025) during 2023 and 2024.

## References

El Abbadi, S. H., Chen, Z., Burdeau, P. M., Rutherford, J. S., Chen, Y., Zhang, Z., Sherwin, E. D., and Brandt, A. R.: Technological Maturity of Aircraft-Based Methane Sensing for Greenhouse Gas Mitigation, *Environ. Sci. Technol.*, 58, 9591–9600, <https://doi.org/10.1021/acs.est.4c02439>, 2024.

Enverus: Drillinginfo and Rig Data, <https://www.enverus.com/solutions/energy-analytics/land/drillinginfo-and-rigdata/>, last access: 17 June 2024.

Hart Energy Mapping & Data Services 2024. <http://rextag.com>, last access: 17 June 2024.

Jervis, D., McKeever, J., Durak, B. O. A., Sloan, J. J., Gains, D., Varon, D. J., Ramier, A., Strupler, M., and Tarrant, E.: The GHGSat-D imaging spectrometer, *Atmos. Meas. Tech.*, 14, 2127–2140, <https://doi.org/10.5194/amt-14-2127-2021>, 2021.

New Mexico Environment Department (NMED): Excess Emission Reports, available at: <https://www.env.nm.gov/air-quality/compliance-and-enforcement/>, 2025, last access: 21 April 2025.

Sherwin, E. D., Chen, Y., Ravikumar, A. P., and Brandt, A. R.: Single-blind test of airplane-based hyperspectral methane detection via controlled releases, *Elem. Sci. Anth.*, 9, 00063, <https://doi.org/10.1525/elementa.2021.00063>, 2021.

Sherwin, E. D., Rutherford, J. S., Zhang, Z., Chen, Y., Wetherley, E. B., Yakovlev, P. V., Berman, E. S. F., Jones, B. B., Cusworth, D. H., Thorpe, A. K., Ayasse, A. K., Duren, R. M., and

This manuscript is a non-peer reviewed preprint submitted to EarthArXiv

Brandt, A. R.: US oil and gas system emissions from nearly one million aerial site measurements, *Nature* 627, 328–334, <https://doi.org/10.1038/s41586-024-07117-5>, 2024.

Sherwin, E., Kruguer, J., Wetherley, E. B., Yakovlev, P. V., Brandt, A., Deiker, S., Berman, E. S. F., and Biraud, S.: Comprehensive Aerial Surveys Find a Reduction in Permian Basin Methane Intensity from 2020-2023, [preprint] <https://dx.doi.org/10.2139/ssrn.5087216>, 2025.

Texas Commission on Environmental Quality (TCEQ): Air Emissions and Maintenance Events, available at: <https://www.tceq.texas.gov/airquality/emission-events>, 2025, last access: 21 April 2025.